Bulletin of Geophysics and Oceanography Vol. XX, n. X, pp. XXX-XXX; Xxxxx 20xx
DOI 10.4430/bgo00543

Spectral analysis of geoelectric data by FFT: application to the exploration of geothermal reservoirs

H. Hami[1], F. Khaldaoui[1], M. Djeddi[3], A. Hocine[1,2], L. Hamai[2] And Y. Djediat[1]

[1] *Geophysics Laboratory, University of Science and Technology Houari Boumediene, Algiers, Algeria*
[2] *Research Center of Astronomy, Astrophysics and Geophysics, Algiers, Algeria*
[3] *Kasdi Merbah University Ouargla, Algiers, Algeria*

(Received: 27 April 2026; accepted: 7 June 2026; published online: 12 November 2026)

ABSTRACT The Electrical Resistivity Tomography (ERT) method is an extensively applied geophysical technique used to map subsurface lithology and fluid distribution. However, the spatial frequency content of the ERT data has historically received little attention compared to other geoelectrical methods, although the conventional interpretation methods, particularly inversion, suffer from the non-uniqueness of the solution. This study proposes a novel interpretation framework for ERT data based on the analysis of their spatial frequency content, transforming apparent resistivity data to frequency domain using the two-dimensional Fast Fourier Transform. Spectral analysis was first applied to synthetic models to characterise the fundamental relationship between the spatial frequency distribution and distinct geoelectrical structures. Furthermore, frequency filtering via a custom Gaussian filter was deployed, enabling the effective delineation of subsurface anomalies. The proposed methodology was subsequently validated using field data from the Hammam Righa hydrothermal system, a prominent geothermal field in the central part of the Tellian Atlas of Algeria. This site was specifically selected due to its complex structural context, where deep-seated faults actively control the circulation and storage of geothermal fluids. These results, compared to inversion, demonstrate that spatial spectral analysis constitutes a powerful complementary tool for enhancing the resolution and interpretation of geoelectrical data.

Key words: resistivity tomography, FFT, geoelectrical, geothermal, spectral analysis.

1. Introduction

Electrical Resistivity Tomography (ERT) is one of the most crucial and versatile imaging methods in applied geophysics, frequently employed to characterise subsoil rock properties (Dastanboo, 2020). In practice, this technique provides a continuous distribution model of electrical resistivity variations across a target region. The variation of subsurface electrical resistivity is primarily governed by fluid dynamics, effective porosity, mineralogy, and the degree of water saturation (Loke, 1999). Given its high potential to identify highly complex subsurface geometries in a non-invasive manner, ERT is widely utilised in geotechnical engineering (Sagar *et al.*, 2021; Avdullahi *et al.*, 2022), hydrogeological mapping (Setiaji, 2023), and hydrothermal systems.

© 2026 - The Author(s)

In this structural context, ERT plays a key role in geothermal exploration by visualising structural variations, fracture networks, fluid saturation, hydrothermal alteration, fluid pathways, and hydrothermal alteration zones, thereby helping delineate the hydrogeological structures governing geothermal systems (Drahor *et al.*, 2014). Geothermal reservoirs (Aliouane and Ouadfeul, 2023) and their associated alteration halos typically exhibit prominent resistivity contrasts relative to the surrounding host rocks. In fact, resistivity levels within active hydrothermal circuits are significantly lower than those of the background matrix. This drop is driven by the presence of high-temperature fluids and networks of open, permeable fractures or faults that easily transmit electrical current through the surrounding high-resistivity formations (Sanjuan *et al.*, 2004). These structures act as preferential pathways for fluid flow rather than as electrical conductors themselves. While increased temperature promotes ion mobility, salinity, saturation, and fluid connectivity remain the main factors controlling the resistivity of the medium.

Despite its proven effectiveness in predicting geological structures, conventional ERT interpretation faces inherent limitations. These are mainly related to the depth-dependent sensitivity and spatial resolution of standard electrode configurations. Since spatial resolution decreases exponentially with depth, fine structural details become blurred, severely limiting the ability to distinguish small-scale features at deep horizons. Furthermore, the numerical inversion algorithms used to process ERT data are severely constrained by the non-uniqueness of the inverse solution and an inherent susceptibility to generate smoothing artefacts, particularly in geometrically complex terrains.

These limitations have encouraged the development and application of other, more robust interpretation methods. However, the interpretation of ERT data is almost exclusively carried out in the spatial domain. In contrast, the spatial frequency content of ERT profiles has been largely overlooked compared to other geoelectrical methods, such as multi-frequency electromagnetic induction (Cassiani *et al.*, 2022), even though frequency-domain analysis is standard in many other branches of geophysics (Saito *et al.*, 2004; Partyka, 2005). Moreover, recent studies demonstrate the critical role of advanced signal processing and spectral analysis in geophysical applications (Doghmane *et al.*, 2022; Ouadfeul and Aliouane, 2023). As a result, this gap highlights a fundamental shortfall in current ERT practice, which is the lack of systematic spatial frequency analysis (SFA).

In this study, we propose a novel approach to analysing the ERT data based on SFA. This approach transforms two-dimensional (2D) resistivity data from the spatial domain to the frequency domain using the 2D Fast Fourier Transform (FFT). This transformation yields a new representation of the signal as a 2D power spectrum and a phase spectrum. Based on the analysis of the generated spectra, it will be possible to improve the quality of the data through frequency filters according to the intrinsic characteristics of the signal. Furthermore, the study aims to highlight the relationship between the spectral energy distribution, as a function of frequency, and the nature of the underlying geological structures.

Unlike conventional ERT data interpretation, which relies on inversion results, frequency analysis by FFT provides complementary information on the spatial organisation of resistivity contrasts. It enables the identification of spectral signatures associated with various geological structures, such as stratified media, faults, and isolated anomalies. Furthermore, FFT offers a simple and effective approach for analysing ERT data and designing frequency filters to enhance the detection of subsurface structures.

To test the proposed approach, a set of ERT sections is generated using synthetic modelling to assess its ability to identify the spectral signatures of certain structures, such as isolated

anomalies and faults. These structures are, then, delineated using band-pass filters. Although this method can be applied in several domains (Dichiarante *et al.*, 2025) involved in ERT data acquisition, its performance is evaluated on field data acquired in the Hammam Righa region, one of the most important in the central Tell Atlas Mountains of Algeria. This geothermal exploration setting is challenging since hydrothermal activity is directly linked to geostructural elements, where faults and fractures play a crucial role as preferential conduits for fluid circulation and heat transfer within geothermal systems. In addition to these complex structures, the reservoirs are often located at great depths and exhibit significant spatial heterogeneity, making conventional geophysical methods ambiguous or prohibitively expensive. Therefore, improving exploration methodologies is a practical necessity to reduce drilling risks, lower development costs, and exploit otherwise inaccessible geothermal resources.

2. Methodological background

2.1. Principles of ERT

The electrical resistivity method involves injecting a constant direct current into the ground between two electrodes, A and B, and measuring the resulting voltage between two potential electrodes, M and N. This potential distribution is subsequently measured on several pairs of electrodes distributed along a profile according to the configuration of the acquisition device (Griffiths and Barker, 1993).

Various data acquisition techniques are employed in ERT studies, depending on the electrode configuration and the objectives of the investigation. The most commonly used configurations include the Schlumberger, Wenner, and dipole-dipole arrays (Saydam and Duckworth, 1978; Dahlin and Zhou, 2004). The observed measurements are, then, converted into apparent resistivity ρ_a [Eq. (1)], which represents a weighted average of the soil's resistance to the passage of current, thus providing a smoothed representation of the actual spatial distribution of the electrical resistivity of the subsoil (Loke *et al.*, 2013):

$$\rho_a = k\frac{V}{I} \tag{1}$$

where V (in volts) is the measured voltage, I (in amperes) is the injected current, ρ_a (in ohm-meters, Ωm) is the apparent resistivity, and k is a geometric factor that depends on the electrode configuration, as described below:

$$k = \frac{2\pi}{\left(\frac{1}{AM} - \frac{1}{AN}\right) - \left(\frac{1}{BM} - \frac{1}{BN}\right)} \tag{2}$$

where *AM*, *AN*, *BM*, and *BN* stand for the distances to the respective electrodes. The final quality of an ERT section depends on both vertical and horizontal resolution, which is determined by electrode spacing, array configuration, measurement density, and target depth. Since resolution decreases with depth, small or thin structures are more reliably imaged in the shallow subsurface, whereas deeper horizons are subject to distortions.

Furthermore, apparent resistivity enables a qualitative prediction of subsurface electrical parameters, but it is insufficient to predict and capture the true spatial distribution and variability of subsurface electrical resistivity (Keller and Frischknecht, 1966).

The inverse problem in ERT is inherently nonlinear and ill-posed, meaning it lacks a unique solution. Several resistivity configurations can produce similar responses, and small errors in the data can lead to large variations in the solution. The classical strategies to reduce non-uniqueness of the solutions to the inverse ERT problem are to solve an optimisation problem using the nonlinear least-squares minimisation technique. This technique considers two components: the first component represents the difference between the resistance values predicted by the inverse ERT model and those measured in the field; the second component is a regularisation term that minimises the roughness of the electrical resistivity model, thus helping to ensure that the inverse problem is well-posed (Gouveia and Scales, 1997; Tarantola, 2005).

Although inverse geoelectric problems are constantly evolving, the results of resistivity profiles reconstructed by inversion still present a smoothed form of the subsurface, in which thin structures and boundaries cannot be highlighted. To overcome this limitation, this study proposes a novel approach aimed at enhancing interpretation accuracy.

2.2. Fast Fourier Transform

One of the most well-known algorithms employed to perform any type of spectral analysis in geophysics is the FFT algorithm (Stork *et al.*, 2014; Silversides, 2020), which can transform information from time or space domain into frequency domain, thus enabling the study of intrinsic signal properties. Initially proposed by Cooley and Tukey (1965), this algorithm provides a clear frequency-domain representation of the signal, facilitating tasks such as spectral analysis and filtering:

$$F(u,v) = \sum_{r=0}^{R-1}\sum_{l=0}^{L-1} f(r,l)e^{-j2\pi\left(\frac{ur}{R}+\frac{vl}{L}\right)} \tag{3}$$

where $F(u, v)$ is the Fourier coefficient at frequency coordinates (u, v), $f(r, l)$ apparent resistivity value at spatial coordinates (r, l), and R and L are the sizes of the 2D input signal matrix.

One of the advantages of the FFT is its efficiency, often reducing computation time by several hundred seconds (Smith, 1999).

It is important to understand the nature of the input signal before performing a spectral analysis. In the case of ERT data, the input signal represents the 2D distribution of ρ_a, which is generally considered a quasi-stationary signal. It is assumed that the electrical properties of the subsurface remain constant during the measurement cycle; therefore, when measurements are performed with direct current, only charge transport by electromigration is measured (Singha *et al.*, 2014). According to Appiah *et al.* (2024), who conducted a comparative study on spectral analysis methods, FFT is best suited for analysing stationary and quasi-stationary signals.

In this study, an FFT-based method is developed to analyse the ERT response. Taking into consideration that the ERT signal is measured at irregular intervals, the signal should be transformed into a regularly sampled sequence of digital data at a defined sampling frequency, f_s, before calculating its spectrum. The choice of the sampling frequency, f_s, must respect the Shannon theorem, which states that the sampling frequency must be at least twice as high as the highest frequency (f_{max}) present in the data:

$$f_s > 2\, f_{max}\,. \tag{4}$$

Applying the FFT to the 2D ERT section produces two spectra. The first is the power spectrum, which shows the energy distribution of each component of the input signal as a function of frequency. The second is the phase spectrum representing the initial angle of each component, thus ensuring the accuracy of position and the sharpness of contours and details during the reconstruction of the filtered data using inverse FFT.

This approach aims to: i) predict the response of certain geological structures by analysing the spectral signature generated by predefined synthetic models; ii) evaluate the resolution of the ERT method in the frequency domain; iii) attenuate random noise typically associated with high spatial frequencies; and iv) perform frequency filtering of the ERT data to highlight its potential as a quantitative tool for improving the interpretation of subsurface structures.

3. Proposed spectral analysis framework

In this section, we present a spectral analysis framework based on the FFT to address the limitations associated with conventional interpretation of ERT data. The proposed approach is based on a unified workflow for the processing and interpretation of ERT data (Fig. 1).

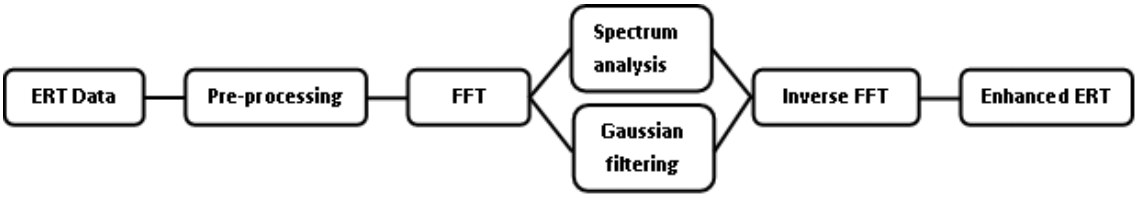


Fig. 1 - Overall workflow of the proposed FFT-based approach.

To evaluate the performance of the method, we use a set of 2D resistivity models representing various underground structures, from which a synthetic dataset is generated. Our strategy involves extracting different plausible modelling scenarios and their associated frequency distributions. The synthetic dataset is created using the Res2DMod modelling tool (Loke, 2002). Subsequently, the same processing method is, then, applied to field data to evaluate their performance.

3.1. Pre-processing

In this step, resistivity data are prepared for spectral analysis. A synthetic dataset is generated for different underground structures, including a layered structure, a fault system, isolated anomalies, etc. The conventional approach involves data evaluation and processing. Usually, data quality is checked and erroneous measurements, due to electrode coupling issues, are eliminated. At this point, an additional preprocessing step, where the resistivity data must be interpolated and resampled at a constant step size before applying the FFT algorithm, is required.

3.2. Application of the FFT algorithm

The preprocessed resistivity data is transformed from the spatial domain to the frequency domain using MATLAB. This transformation produces a power and a phase spectrum, where the

amplitude reflects the signal intensity at a given frequency and the phase represents the spatial arrangement of anomalies.

3.3. Spectrum analysis

The resulting power spectrum is, then, analysed both qualitatively and quantitatively. A qualitative assessment is first performed to evaluate the quality of the data, particularly in terms of noise and its influence on the spectrum. Then, we analysed the spectral patterns that define each of the geological structures. This could enable to predict the presence of certain geological features. The quantitative analysis involves the determination of the band-pass frequency range (as explained in the following section) as well as the dominant frequency. These frequencies will serve as parameters for creating the Gaussian filter.

3.4. Gaussian filtering

The proposed technique is based on the design and application of a Gaussian low-pass filter based on the quantitative attributes of the power spectrum to be filtered. This filter is characterised by a Fourier transform that remains Gaussian and whose spatial expressions do not contain negative values (Fig. 2a). By defining the bandwidth to encompass the dominant low-frequency lobe, defined here as containing -3 dB of spectral energy (Fig. 2b), the filter effectively acts as a signal amplifier (Cooley and Tukey, 1965).

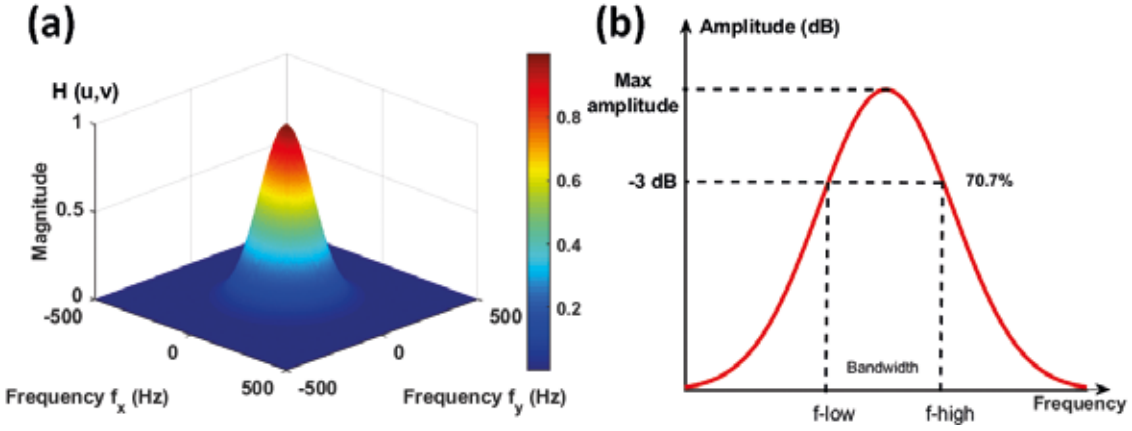


Fig. 2 - a) Gaussian filter response in frequency domain. b) Schematic representation of a typical frequency spectrum illustrating the selected bandwidth range.

The filter is defined in the frequency domain as follows:

$$H(u,v) = e^{-\frac{D^2(u,v)}{2\sigma^2}} \text{ with } \quad D(u,v) = \sqrt{u^2 + v^2} \tag{5}$$

where $D(u, v)$ is the distance between the original point in the frequency domain and point (u, v). Parameter σ is used to measure the width of the Gaussian curve, letting $\sigma = D_0$, where D_0 is the cutoff frequency. When $D(u, v) = D_0$, the filter drops to 0.707 of the maximum value (Qu *et al.*, 2012).

The bandwidth range is defined as the frequency span between the two points where the spectrum crosses the -3dB level, as illustrated in Fig. 2. The cutoff frequencies correspond to the points encompassing 70% of the total spectral energy of the signal. This approach ensures an objective and reproducible application of the Gaussian filter. Wide bandwidth filters are sensitive to noise.

Defining the bandwidth of the ERT section, then multiplying the power spectrum term by term by the resulting Gaussian filter, results in a smooth filtered power spectrum carrying the signature of anomalous or dominant underground structures.

3.5. Inverse FFT and structural feature extraction

After filtering in the frequency domain, an inverse Fourier transform is applied to reconstruct the resistivity section in the spatial domain. The resulting filtered ERT profile enables a preliminary qualitative estimation of the resistivity anomalies present in the subsurface, highlighting contour lines converging towards the centre of the anomalies. Therefore, the general trend of localised anomalies can be distinguished.

To refine the delineation of the structures, a Laplacian operator is applied to the filtered section [Eq. (6)], providing better delineation of the anomaly shapes:

$$\begin{bmatrix} 0 & -1 & 0 \\ -1 & 4 & -1 \\ 0 & -1 & 0 \end{bmatrix}. \tag{6}$$

Eq. (6) represents the discrete approximation commonly used for the Laplacian filter.

In fact, the Laplacian operator enables to localise the inflection points of the anomaly, which correspond to its actual boundaries (Zheng and Sun, 2008). A final thresholding step (ImochaSingh *et al.*, 2012) is performed on the results of the Laplacian-transformed section to quantify the contours of the principal anomalies:

$$T(x,y) = m(x,y) + k \times \delta(x,y) \tag{7}$$

where $T(x, y)$ is the threshold value, $m(x, y)$ is the local mean, and $\delta(x, y)$ is the standard deviation of the filtered section. k is a bias and set as k =1.

4. Spectral response analysis using synthetic models

In this section, the spectral contents of five synthetic ERT models were analysed. These models represent typical subsurface structures, including i) a uniform half-space, an isolated anomaly, and a layered structure (Fig. 3); ii) a fault model and a hydrothermal system model (Fig. 4).

The objective is to establish a reference framework for the interpretation of spectral signatures and comparison of synthetic responses with field data. To simulate measurement uncertainties and approximate real-world conditions, a random noise level of 5% was incorporated into the synthetic resistivity data.

4.1. Uniform half-space, isolated anomaly, and layered model

Fig. 3 shows analysis results with 2D FFT performed on the ERT sections of the three synthetic models: a) a uniform half-space, b) an isolated anomaly, and c) a stratified model. Each model is represented by three panels: synthetic structures, the generated ERT sections with 5% added noise, and the resulting power spectrum. The centre of the spectrum represents a zero frequency, also called the offset. Frequency components increase with distance from the centre, enabling a clear distinction between low- and high-frequency contributions to the input signal.

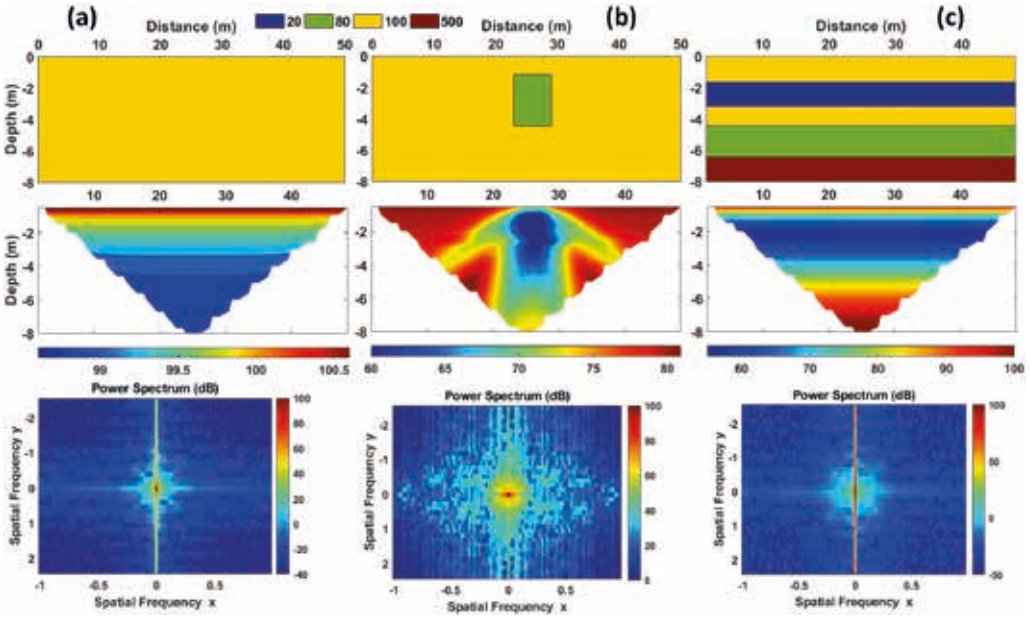


Fig 3 - Pattern analysis results of the FFT performed on the ERT sections of three synthetic models: a) uniform half-space, b) isolated anomaly, and c) layered model. Top panel: synthetic structures of analysed patterns. Middle panel: generated ERT sections with 5% of noise added. Bottom panel: power frequency spectra generated with 2D FFT.

For the uniform half-space (Fig. 3a), the power spectrum exhibits a high energy concentration at zero frequency, reflecting the homogeneity of the model. The rapid decay of spectral energy from zero confirms the absence of structural contrasts or anomalies within the model. The vertical line in the *y* direction of the spatial frequencies corresponds to the direction of current propagation, the intensity of which decreases with depth. The noise component is characterised by low energy scattered towards high spatial frequencies, approximately $fx > 0.5\ m^{-1}$ and $fy > 1\ m^{-1}$.

The isolated anomaly (Fig. 3b), on the other hand, creates wider spectral responses because of the difference in their resistivity compared to the surrounding medium, which exhibits more extensive dominant spectrum at low spatial frequencies.

The layered model (Fig. 3c) exhibits a predominance of low spatial frequencies, characterised by a vertical high energy trend approaching $fx = 0$, which correlates with the sudden change in resistivity between layers. The high spatial frequencies seem to be attenuated by formations in the first few metres. A small variation in spectral energy is also observed in the direction of $fy = 0$, indicating a small lateral variation in resistivity, suggesting the presence of large-scale smooth structures.

4.2. Faulted and hydrothermal system models

The last two synthetic models are created to simulate a geothermal setting composed of several key geological and physical elements that control the storage and circulation of hot groundwater (Fig. 4).

The first model represents a conductive fault with a dip of 60° and a displacement of approximately 3 m, while in the second model, the fault extends downwards into a thermal reservoir characterised by a low resistivity of 15 Ωm. The fault-reservoir system is surrounded by an alteration halo resulting from the hydrodynamic interaction, with a moderate resistivity of 30 Ωm.

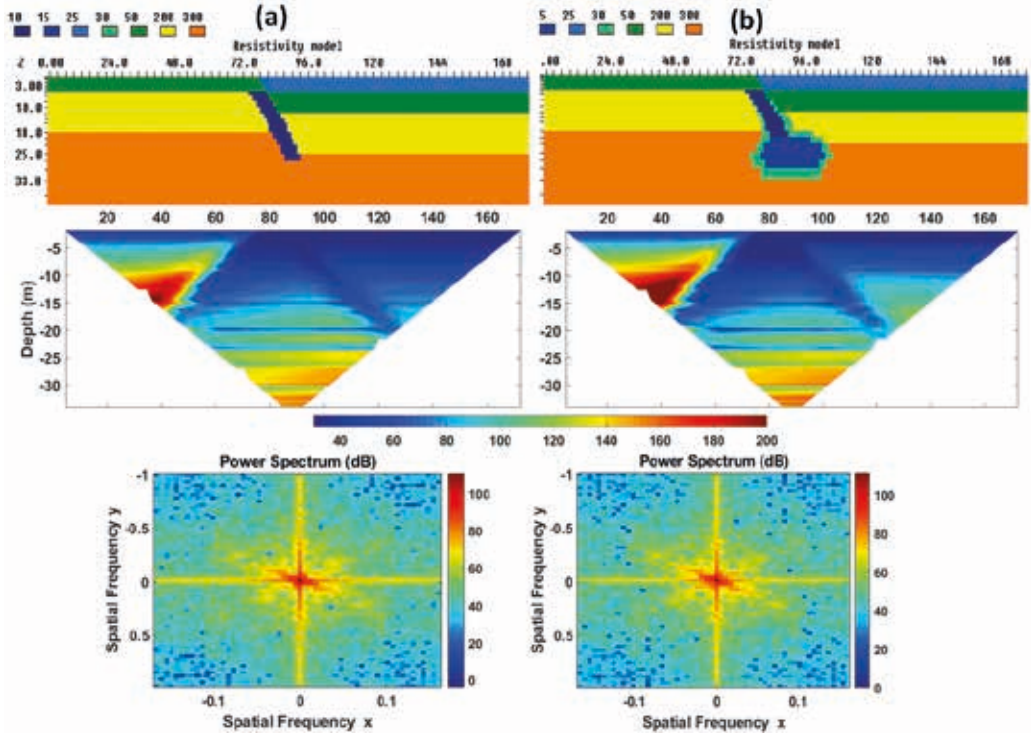


Fig 4 - Result of FFT-based pattern analysis applied to the ERT sections of two synthetic models: a) fault model; and b) hydrothermal system model. Top panel: synthetic structures. Middle panel: simulated ERT sections with 5% of added noise. Bottom panel: 2D FFT power spectra.

The fault model in Fig. 4a shows a power spectrum with a strong cross-shaped structure along the horizontal and vertical frequency axes. The vertical component ($fx = 0$) reflects variations in resistivity with depth, while the horizontal component ($fy = 0$) is associated with lateral resistivity contrast induced by the fault contact.

The hydrothermal system model (Fig. 4b) shows a spectral response almost identical to that of the fault model (Fig. 4a); the only significant difference is related to the fact that the horizontal component has lower values ($fy = 0$). This difference is due to the presence of the alteration halo, which leads to reduced resistivity contrasts between the fault and the other layers (Fig. 4b). The strong resistivity contrast between the fault and the other horizontal layers resulted in high spectral energy (Fig. 4a).

4.3. Frequency analysis and filtering

Table 1 shows the dominant frequencies and the bandwidth ranges for each synthetic model. The dominant frequency is always close to zero, reflecting the overall resistivity trend of the models. On the other hand, the bandwidth changes significantly depending on the structural complexity of each model. To further evaluate the performance of the proposed methodology, a quantitative metric evaluation based on the root mean square error (RMSE) indicator compares the structural model obtained after filtering to the synthetic model.

Extensive or large-scale structures such as uniform half-spaces and multilayer models exhibit a wide bandwidth that can be associated with a medium of low lateral heterogeneity, while isolated, or small-scale structures such as faults and fractured media exhibit a narrower bandwidth.

Table 1 - Dominant frequencies, bandwidth ranges, and RMSE values for each synthetic model.

Model	Dominant frequency (m^{-1})	Bandwidth range (m^{-1})	RMSE (m)
Uniform half-space	0.0	[-0.81; 0.02]	0.3
Isolated anomaly	0.0	[-0.21; 0.09]	0.38
Layered model	0.0	[-0.66; 0.28]	0.31
Fault model	0.0	[-0.07; 0.04]	0.7
Hydrothermal system	0.0	[-0.07; 0.04]	1.2

The power spectrum is filtered by multiplying it by a transfer function defined in the frequency domain. A Gaussian filter is adopted due to its smooth attenuation properties and its ability to reduce spectral artefacts.

To preserve the central part of the power spectrum, which exhibits a high energy concentration near $fx = 0$, a Gaussian low-pass filter is applied. The cutoff frequency, f_cutoff, is defined as the upper limit of the retained frequency band, ensuring attenuation of higher frequency components while preserving the dominant low-frequency energy.

Fig. 5 shows an example of the power spectrum in the case of a shallow isolated anomaly, before and after application of the Gaussian filter.

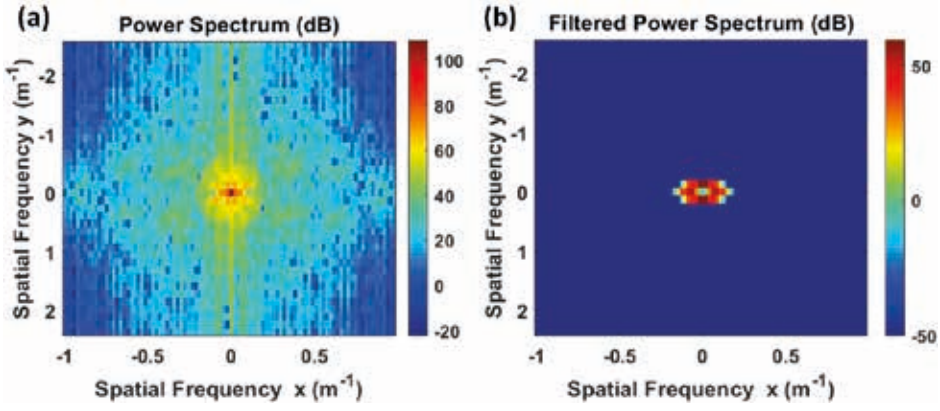


Fig. 5 - a) Power spectrum of a shallow isolated anomaly, b) filtered power spectrum $f_cutoff = 0.21\ m^{-1}$.

4.4. Reconstruction and structural delineation

An inverse FFT is applied to the filtered spectrum to obtain the respective ERT sections (Fig. 6). The resulting ERT sections highlight the position of the dominant structural anomalies. Although the Gaussian filter section provides accurate delineation of the anomaly shapes, the exact location of its boundaries remains dependent on gradient variations. Therefore, the application of a Laplacian operator will provide a more precise quantification of the structure boundaries.

Although the Laplacian operator proved effective for highlighting structural boundaries, it remains sensitive to high-frequency noise and, compared to other edge detection techniques such as gradient-based operators, may locally amplify artefacts. It should also be noted that the FFT and Gaussian filtering procedures applied to apparent resistivity pseudo-sections significantly attenuate high-frequency noise. Consequently, the resulting filtered anomalies do not constitute physically constrained resistivity models. Therefore, the comparison with conventional inversion results remains essential to assess the geological consistency and physical significance of the detected structures.

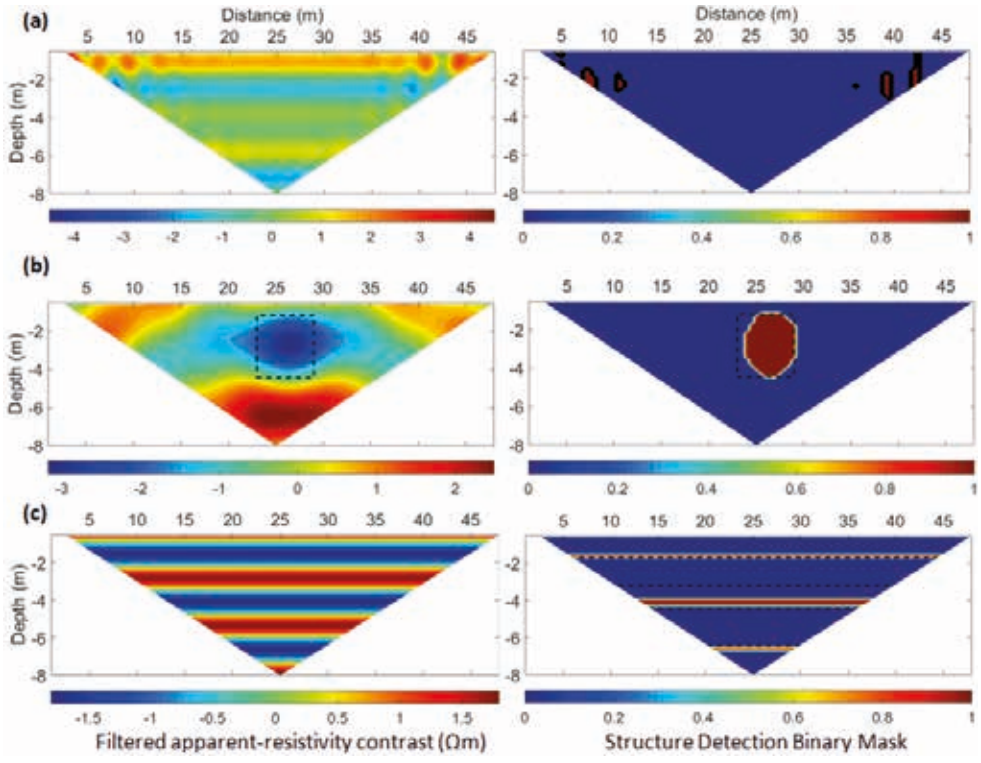


Fig. 6 - Inverse FFT of the filtered power spectrum for different synthetic models: a) uniform half-space, b) isolated anomaly, and c) layered model. Left panel: filtered ERT sections. Right panel: structural boundaries detected using a thresholded Laplacian operator of panels a, b, and c.

In the case of a uniform half-space (Fig. 6a), the application of the Laplacian operator reveals a uniform environment with no major anomalies, except for some variations due to edge effects. On the other hand, the isolated anomaly (Fig. 6b) shows contour lines converging towards the conductive body, revealing a well-defined shape. Furthermore, the Laplacian operator provides

an accurate localisation of its boundaries with an RMSE value of 0.38 m (Table 1).

For the layered model (Fig. 6c), the filtered ERT section shows a strong linear trend compared to the uniform model due to the sharp resistivity contrast between layers. Furthermore, the application of the Laplacian operator enhances the detection of contact interfaces with an RMSE value of 0.31 m. However, the resolution limitations of the ERT method do not enable the precise determination of the deep contact boundaries.

Applying the low-pass filter [0.00; 0.04 m^{-1}] to the fault model reveals the presence of a subvertical discontinuity, corresponding to the fault location. Furthermore, the fault displacement is clearly quantified. The thicknesses of the upper layers are determined more accurately than those at greater depths (Fig. 7a). This results from the fact that resolution decreases with depth.

The anomalies highlighted by the high-pass filter [0.05; 0.08 m^{-1}] correspond to the boundaries between layers (Fig. 7b). The fault was manifested by a discontinuity in the interface boundaries.

In the hydrothermal system model, the alteration halo acts as a filter, attenuating the resistivity contrast between the fault and the surrounding formations. This is clearly visible in the low-pass filtered section [0.00; 0.05 m^{-1}] (Fig 7a). The fault-reservoir and alteration-halo system appears as a single elongated structure aligned with the fault direction (Fig. 7c).

The high-pass filter [0.04; 0.07 m^{-1}] clearly highlighted the contact boundaries between the stratigraphic layers, as well as the top and bottom of the reservoir (Fig. 7d). Comparison of the obtained model with the initial synthetic model shows a slightly higher RMSE (1.2 m) than that of the fault model (0.7 m).

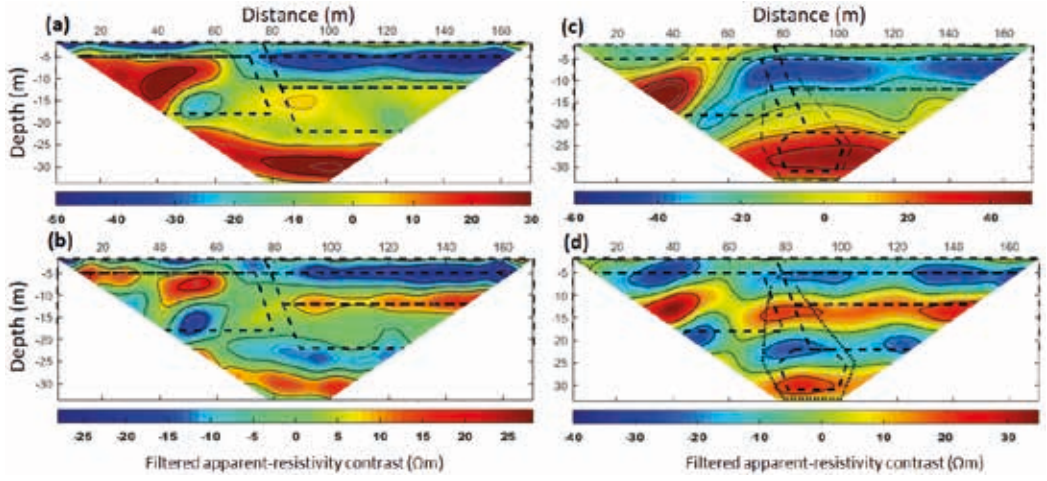


Fig. 7 - Inverse FFT of the filtered power spectrum: a) low-pass filtered ERT section for the fault model, b) high-pass filtered ERT section for the fault model, c) low-pass filtered ERT section for the hydrothermal system model, and d) high-pass filtered ERT section for the hydrothermal system model.

5. Application to field data: Hammam Righa geothermal system

5.1. Geological and geothermal setting

The Hammam Righa site is located in northern Algeria (Fig. 8), within the Tell Atlas Mountains, a segment of the Maghreb Alpine chain formed by the convergence of the African and Eurasian plates (Durand-Delga and Fontboté, 1980; Wildi, 1983). This region is characterised by a complex

geology marked by compressive tectonic phases, significant seismic activity, and associated post-collision volcanism (Meghraoui, 1988; Maury *et al.*, 2000).

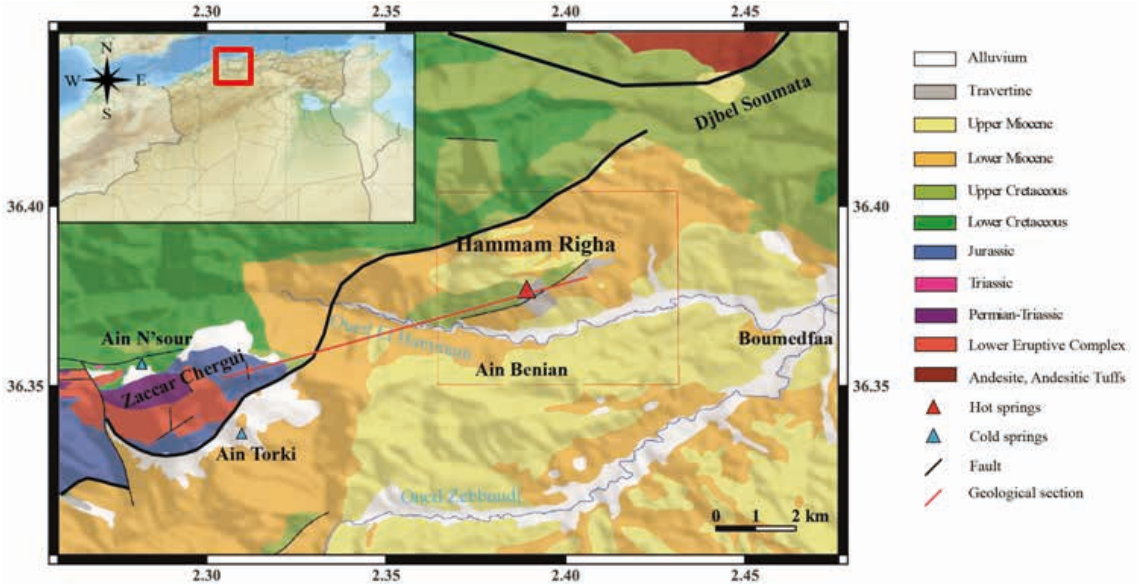


Fig. 8 - Geological map of the Hammam Righa site (after Bouchareb-Haouchine *et al.*, 2012).

The study area lies at the transition between the Neogene Mitidja Basin to the NE and the Upper Chelif Basin to the SW, in a highly deformed structural zone where tectonic faults play a crucial role in fluid circulation.

Lithostratigraphically, the region presents a succession of formations ranging from the Palaeozoic to the Quaternary periods. The Jurassic carbonate formations, consisting mainly of fractured limestones, represent the main geothermal reservoir, in accordance with regional models of hydrothermal systems in Algeria (Issaadi, 1992; Belhai, 1996; Saibi *et al.*, 2006; Saibi, 2015). These formations rest on a relatively impermeable substrate and are covered by Cretaceous and Miocene marl-limestone and detrital formations, characterised by strong lithological and structural heterogeneity.

The Miocene deposits, extensively developed in the Hammam Righa Basin, bear witness to sedimentary evolution controlled by Alpine tectonic movements and are affected by folding and faulting related to regional compression (Guigue, 1947; Perrodon, 1957).

The tectonic structure is dominated by a dense network of faults, mainly oriented NE–SW, corresponding to deep-seated faults inherited and reactivated during the various Cenozoic tectonic phases. These structures are essential to the functioning of the hydrothermal system by ensuring connectivity, as they provide the hydraulic link between the deep reservoir and the surface, and by controlling the upwelling of thermal fluids.

This role of faults as preferred conduits was well documented in geothermal systems worldwide (Sibson, 1996; Curewitz and Karson, 1997). Furthermore, the presence of Triassic evaporite formations and evidence of Miocene volcanism suggests the existence of a heat source linked to magmatic intrusions, contributing to the heating of deep circulating waters (Hernandez and Lepvrier, 1979; Maury *et al.*, 2000).

Thus, the geological context of Hammam Righa results from the interaction between complex stratigraphy, active tectonics, and magmatic processes, creating a particularly favourable environment for the development of a hydrothermal system controlled by tectonic structures and the properties of deep carbonate formations (Fig. 9). This configuration is consistent with conceptual models of geothermal systems of active margins and collision chains (Hochstein, 1990; Dickson and Fanelli, 2011).

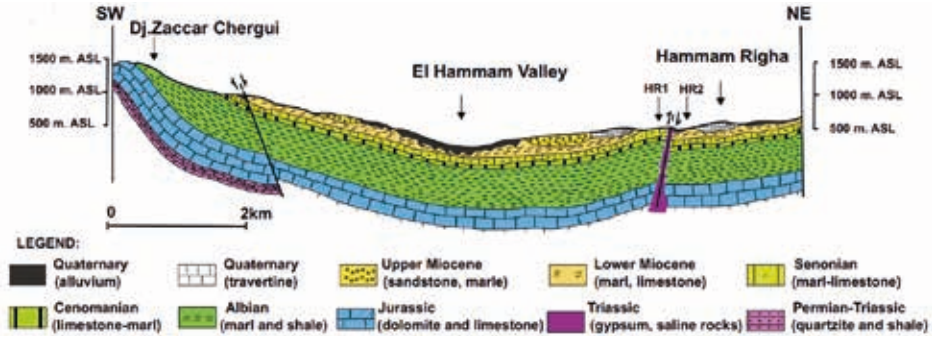


Fig. 9 - Geological section of the study area (after Belhai *et al.*, 2016)

5.2. Data acquisition

Electrical resistivity data were acquired at the Hammam Righa geothermal site using three 2D ERT profiles, namely P1, P2, and P3 (Fig. 10). The surveys were carried out using the Terrameter LS2 resistivity meter with a dipole-dipole array. This array was chosen for its superior horizontal resolution. A minimum electrode spacing of 10 m was used for all three profiles, more specifically approximately 230 m for profiles P1 and P2, and 470 m for profile P3.

Profiles P2 and P3 are oriented in a NE–SW direction, and profile P2 in a NW–SE direction, approximately 50 m from wells B1 and B2, drilled in 1968 by GEMP (Groupe d'Études sur

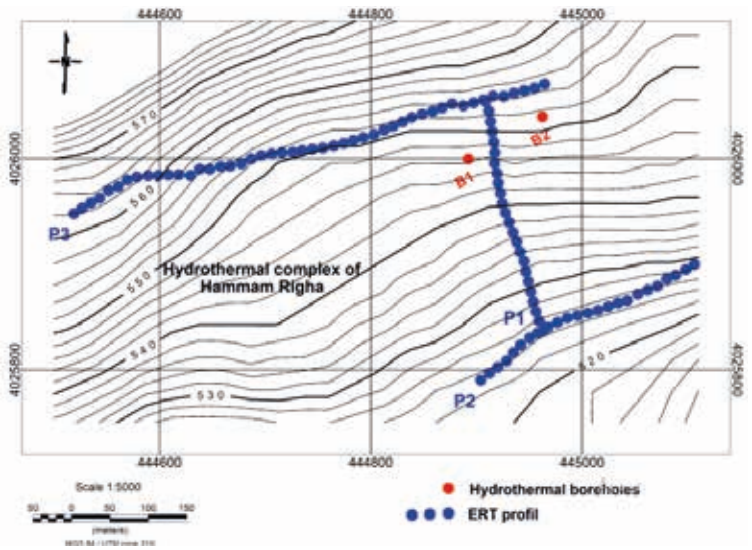


Fig. 10 - Topographic map of the Hammam Righa hydrothermal complex showing the location of the ERT profiles (P1, P2, and P3) and hydrothermal boreholes (B1 and B2).

les Milieux Poreux – Research Group on Porous Environments) at ancient springs, through Quaternary and Miocene formations (Hocine *et al.*, 2024).

5.3. ERT data and spatial distribution

Profiles P1 and P2 show a significant resistivity contrast between the near surface and deeper levels. A high-resistivity surface layer (100 Ωm) extends to a depth of approximately −10 m, suggesting dry or compact surface materials (Fig. 11). In profile P1, lateral heterogeneity is observed at the shallow depth, suggesting an abrupt lithological change.

Beyond a depth of approximately −15 m, both profiles are dominated by a conductive zone (~20 Ωm). This signature is often associated with water-saturated zones, clays, or marl units.

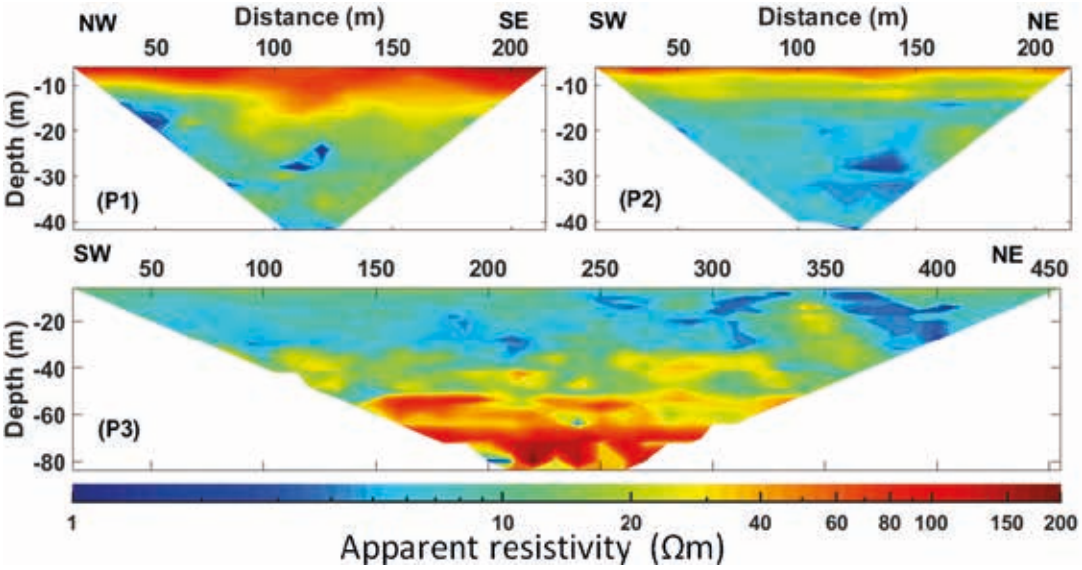


Fig. 11 - Pseudo-sections of the measured apparent resistivity for profiles P1, P2, and P3.

Profile P3 shows the surface and intermediate zones from the surface to approximately −60 m, characterised by low resistivity values (< 20 Ωm), indicating a predominantly conductive subsurface (Fig. 11).

At depth, a resistive anomaly (> 100 Ωm), which is often indicative of compact rock, is observed. The sharp localised anomalies observed at −80 m of depth are interpreted as artefacts related to measurement noise. The dipole-dipole device is characterised by high sensitivity to noise.

5.4. Spectral analysis of ERT data

The power spectrum obtained by transforming the ERT data into frequency domain shows a dominance of low spatial frequencies, reflecting large-scale resistivity variations (Fig. 12).

For profile P1, the energy is strongly concentrated at low frequencies ($fx < 0.03$ m^{-1}) with a marked cross-shaped structure along the horizontal and vertical frequency axes (Fig. 12a). This

pattern is similar to the one seen in the synthetic fault model and indicates the presence of subvertical discontinuity (Fig. 4a). However, due to the limited lateral resolution of the recorded data, it is difficult to highlight small-scale contacts in raw data.

Profile P2 shows a significantly low energy distribution at high frequencies (Fig. 12b). This indicates low contamination by random noise and an absence of small-scale geological anomalies. The vertical high-energy trend approaching $fx = 0$ is identical to the one observed in the stratified model (Fig. 3c), suggesting a strong resistivity contrast between large-scale layers.

Profile P3 shows a high concentration of energy at low spatial frequencies that gradually attenuates towards higher frequencies (Fig. 12c). This Gaussian shape distribution of energy is similar to the synthetic model of the isolated anomaly (Fig. 3b). Energy scattered towards high spatial frequencies, approximately ($fx > 0.5$ m^{-1} and $fy > 1$ m^{-1}), can be an indicator of the presence of random noise, which explains the sharp, distinct peaks observed in the pseudo-section.

A visual analysis of the power spectra of pseudo-sections P1, P2, and P3 enabled us to identify the main area of energy concentration around the dominant frequency. Frequencies corresponding to a significant decrease in spectral energy were selected as the bandwidth limits. This approach enables us to select frequencies associated with the main geological structures while excluding high-frequency components generally linked to noise or spatially limited heterogeneities.

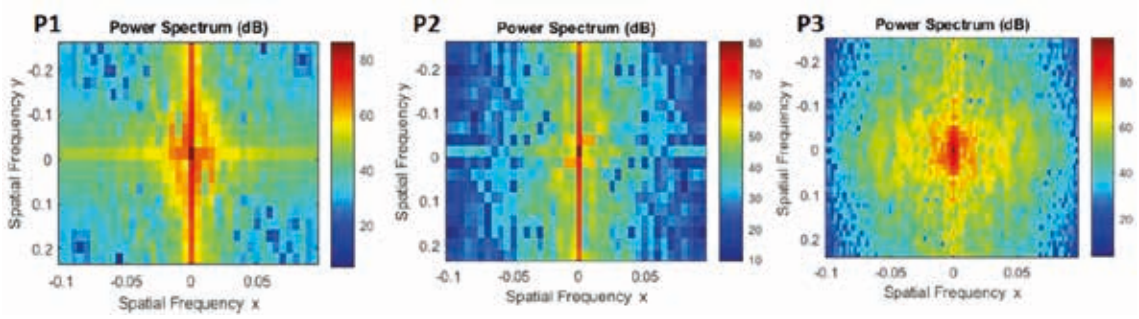


Fig. 12 - Power spectrum of pseudo-sections: a) profile P1, b) profile P2, and c) profile P3.

5.5. Spectral filtering results

A low-pass filter was applied to the spectral domain of the three profiles (Fig. 13a), based on the bandwidth ranges (Table 2) to preserve the useful frequency content while removing random noise generally associated with high frequencies.

The filtered ERT sections provide an image of the subsurface with improved clarity.

Table 2 - Spectral filtering parameters for each profile.

Profile	Bandwidth range (m^{-1})	Low-pass filter	High-pass filter
P1	[−0.1; 0.04]	[0.0 ; 0.04]	[0.04 ; 0.1]
P2	[−0.1; 0.03]	[0.0 ; 0.03]	[0.03 ; 0.1]
P3	[−0.08; 0.03]	[0.0 ; 0.03]	[0.03 ; 0.08]

The 2D power spectrum exhibits central symmetry around zero. Therefore, the cutoff frequency of the low-pass filter corresponds to the minimum absolute value of the bandwidth limits. The maximum absolute value corresponds to the cutoff frequency of the high-pass filter.

Profiles P1 and P2 (Fig. 13a), obtained from low-pass filtering, reveal a shallow layer (0 to −10 m) with high resistivity that varies laterally (Zone 1), followed by an intermediate zone extending to approximately −20 m. A second structure, extending laterally (−20 to −40 m), could be a confined aquifer or a clay formation (Zone 2). A certain structural continuity (Zone 1 and Zone 2) is observed between the two profiles.

In profile P3, the superficial layer (Zone 1) appears eroded, exposing Zone 2 at the surface. A deeper conductive zone extends down to −60 m, resting on a resistive structure interpreted as the bedrock (Zone 4).

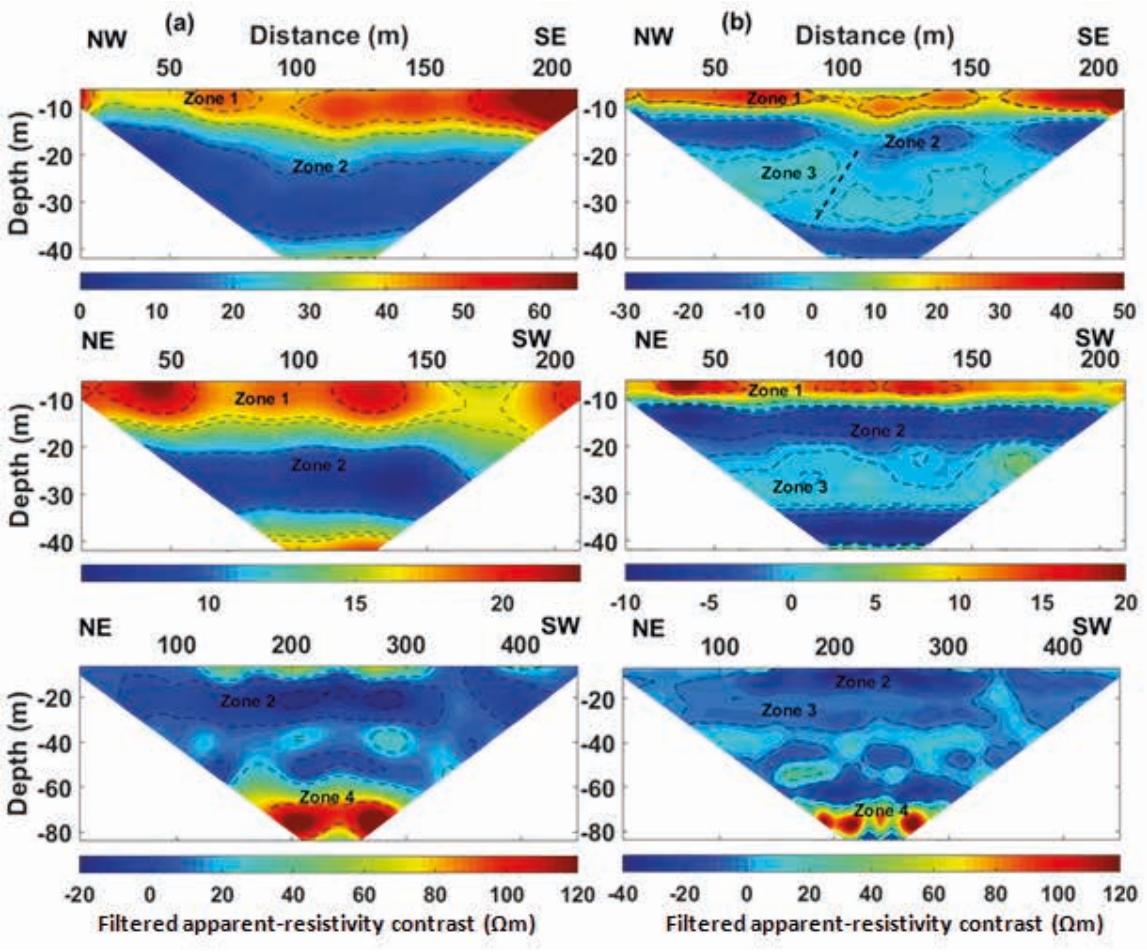


Fig. 13 - Spectral filtering results for: a) low-pass filtered sections, and b) high-pass filtered sections. Top panel: profile P1. Middle panel: profile P2. Bottom panel: profile P3.

5.6. Geological interpretation

From a structural perspective, previous studies conducted in the Hammam Righa region (Ripelin *et al.*, 1903) showed that the thermal springs are controlled by a major NE–SW fault, a direction perpendicular to the direction of profile P1 (Fig. 8), connecting Senonian and Cartesian. Vertical electrical sounding surveys further reveal a system of shallow faults (Hocine *et al.*, 2024).

The spectral response observed in profile P1 confirmed the presence of a subvertical contact. Furthermore, the high-pass filter results revealed a discontinuity zone at the Cretaceous level (20–30 m), likely associated with faulting (Fig. 11b).

The stratigraphic units obtained from low-pass filter analysis coincide well with earlier interpretations in the literature (Hocine *et al.*, 2024):

- Zone 1 (0–10 m) with high variable resistivity, corresponding to travertine deposits;
- Zone 2 (10–30 m), with very low resistivity (3 to 8 Ωm), representing a clay-marl formation (Miocene);
- Zone 3, with moderate resistivity attributed to dolomite;
- Zone 4 (>60 m), marl-limestone-dolomitic bedrock (Cretaceous) characterised by high resistivity.

Profile P3 indicates that the travertine deposits (Zone 1) have been eroded, exposing the clay-marl unit (Zone 2) to the surface (Fig. 13a).

Although the depth of investigation of profiles P1, P2, and P3 does not enable to access the reservoir levels, the presence of faults is evidenced by the spectral response of profile P1, oriented perpendicular to the NE–SW direction of the fault. It is important to note that the orientation of profiles P2 and P3, parallel to the fault, is not optimal for fault mapping.

5.7. Comparison and validation of results by inversion

To evaluate the performance of the proposed method, electrical resistivity profiles P1, P2, and P3 were inverted using the RES2DINV software to compare the inverted model with the results obtained by frequency filtering. The inversion process uses L1-based least-squares optimisation to limit the influence of outliers and data noise (Schmidt, 2005). The model discretisation is initialised using a direct finite element forward solver. After five iterations, we obtained the inverse resistivity models with absolute errors of 8.49%, 7.91%, and 11.59% for the three profiles P1, P2, and P3, respectively. These high RMSE values are primarily due to the noisy recorded data, which contains numerous erroneous values.

The interpretation of the inverted ERT profiles presented different resistivity zones, indicating diverse subsurface lithologies (Fig. 14). The results show a resistive cover layer approximately 10 m thick and of high resistivity (40 to 100 Ωm), present along the entire length of profiles P1 and P2 near the surface (Zone 1).

Immediately below this cover layer, a zone of relatively medium resistivity, ranging from 8 to 20 Ωm, was identified at a depth of 10 to 30 m. This corresponds to Zone 2 defined in the filtered sections. This zone is also observed in the upper part of profile P3, where Zone 1 appears to be eroded.

Zone 3 corresponds to a formation of low electrical resistivity (<10 Ωm) at a depth of 20 m. It exhibits a clear lateral discontinuity that may be associated with a fault.

The inverted P3 profile suggests a multilayered subsurface structure:

- Zone 2: a shallow conductive cover, interpreted as altered and/or water-saturated formations;

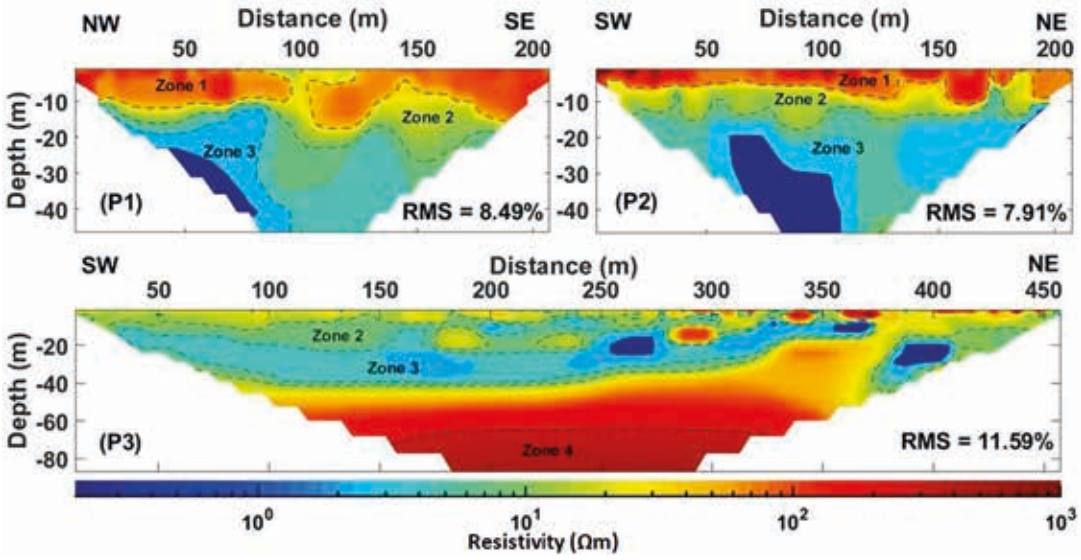


Fig. 14 - Inversion results for profiles P1, P2, and P3.

- Zone 3: several localised conductive anomalies and strong lateral resistivity contrasts indicate the possible presence of fluid flow pathways that could correspond to hydrothermal alteration zones (250–320 m) and (380–420 m);
- Zone 4: a deep resistive basement extending over most of the profile.

Comparison between the inverted and filtered profiles reveals a certain similarity between the defined zones, especially near the surface.

Both inversion and frequency filtering methods clearly delineate several anomalies located in the upper layers (Zone 2 and Zone 3). Conversely, at depth, inversion provides a smoother representation of the basement in the case of profile P3, which extends to the surface (350–430 m) with a nearly vertical and smooth structure (Zone 4). Meanwhile, the filtered section reveals several structural discontinuities extending from the basement to the surface, which could represent preferential fluid flow pathways.

The vertical discontinuity delimiting Zone 3 in the inverted P1 profile is also clearly marked on the high-frequency filtered P1 section, which further enhances the delineation of localised structures. Thus, the high-pass filter significantly improves the identification of boundaries, faults, and structures.

6. Discussion and validation of the spectral approach

This study presents a new methodology for interpreting geoelectrical data, which aims to identify and locate bodies and discontinuities in the subsurface based on the spectral response of the measured signal.

Synthetic models revealed that different geological configurations produce distinct spectral signatures. In particular, fault-type features exhibit a unique cross-shaped energy distribution in the frequency domain, while stratified layers and isolated geological anomalies exhibit signatures characterised by low frequencies.

Furthermore, we were able to characterise the structural boundaries and contact depths of buried bodies, as well as clear lateral discontinuities, from the filtered frequency profiles, thus improving the mapping of geological structures.

The quantitative assessment of the proposed method's performance on the synthetic data revealed comparatively low RMSE values (0.3–1.2 m) in estimating the structural boundaries of the formations compared to the initial models.

To test the proposed method, we implemented it in a geothermal study in the Hammam Righa region. The results obtained by filtering resistivity data in the frequency domain are consistent with the results of previous work carried out in the Hammam Righa region. From a geological perspective, the proposed method provides a reliable estimation of the thickness of geological layers, which is confirmed by the interpretation results obtained from old boreholes in the region. High-pass filters also enable the delineation of fine structures and lateral discontinuities. Filtering the raw data, while respecting bandwidth-related criteria, has contributed to attenuating random noise.

The results obtained at Hammam Righa show that frequency analysis makes it possible to: i) identify characteristic spectral signatures associated with certain geological structures, including faults and lithological contacts, ii) improve the detection of lateral discontinuities through spectral filtering, iii) reduce the influence of random noise present in the data, and iv) provide useful information that can be subsequently integrated as constraints in the inversion process.

The comparison performed (see Section 5.7) between the filtered pseudo-sections and the inverted resistivity models shows that the main geological structures, including layer boundaries and structural discontinuities, are consistently preserved. Although the present validation is primarily qualitative, it confirms the geological validity of the proposed spectral filtering approach and its ability to improve the interpretation of the ERT data while improving the readability of ERT pseudo-sections. Future work will focus on quantitative assessment based on statistical metrics and on the inversion of filtered datasets to further evaluate the performance of the proposed methodology.

Although this method has yielded accurate results, it remains dependent on acquisition parameters, which have a significant impact on data quality and spatial resolution. The proposed analysis technique is not only an innovative and useful method in itself but also a tool for improving the contours of electrical anomalies.

Future prospects include the application of the results obtained to constrain the solution during the inversion process, thus helping to resolve the ambiguity inherent in the inverse resistivity problem.

7. Conclusions

This study implemented an innovative approach based on the spectral analysis of electrical resistivity data to improve the interpretation of subsurface geological structures. The use of the 2D FFT provided a means to characterise the frequency content of the ERT pseudo-sections and to identify subsurface structure from the spectral response of the measured signal.

The spectral analysis of the synthetic models showed that each structure (homogeneous medium, isolated anomalies, stratification, fault, hydrothermal system) produces a distinct spectral response. The application of a frequency filter, in particular low-pass and high-pass Gaussian filters, enhanced structural delineation by reducing the effect of noise.

The application of the method on data recorded from the Hammam Righa hydrothermal system confirmed the effectiveness of this approach. The results were consistent with the geological and hydrothermal context of the study area, particularly the identification of the conductive zones corresponding to marl formations and resistive zones associated with carbonate formations. Spectral analysis also revealed structural discontinuities related to faulting controlling the geothermal system.

Comparing the results obtained using the proposed method in the Hammam Regha region with those obtained using conventional inversion demonstrated the effectiveness of spectral analysis and frequency filtering in structurally interpreting electrical resistivity tomography data.

Nevertheless, certain limitations should be pointed out. The measurement result strongly relies on the acquisition parameters, as well as the sensitivity of the dipole-dipole array, while its main advantage is its ability to model geological structures in a relatively simple and more realistic way.

Despite these limitations, the proposed approach constitutes a supplementary tool for analysing geoelectrical data, thus allowing for better characterisation of geological structures and geothermal systems.

Future perspectives will focus on the application of this approach to other regions with diverse geological characteristics to validate its effectiveness and explore its applicability in other geoelectric exploration contexts. In addition, this will include integrating this approach into constrained inversion processes and extending it to three-dimensional resistivity data. The combined use of artificial intelligence methods could further enhance the interpretation of geoelectrical data.

Acknowledgments. The authors gratefully acknowledge the opportunity to present this work at the International Conference on Fossil and Renewable Energies ICFRE 2025. The constructive comments and insightful discussions with the conference participants have helped improve the quality of this manuscript. The authors wish to thank the anonymous reviewers and the editor for their helpful remarks and suggestions that enabled the paper to be improved.

REFERENCES

Aliouane L. and Ouadfeul S.A.; 2023: *Geothermal energy in Algeria and the contribution of geophysics.* In: Proc. 1st International Conference on Physics of Semiconductor Devices, Renewable Energies and Environment. Phys. Sci. Forum, 6, doi: 10.3390/psf2023006002.

Appiah M.K., Danuor S.K. and Bienibuor A.K.; 2024: *Performance of continuous wavelet transform over Fourier transform in features resolutions*. Int. J. Geosci., 15, 87-105.

Avdullahi S., Reci H., Lika J., Perolli F. and Shabani F.; 2022: *Geotechnical-geophysical investigations in the Mbuji-Mayi region, Congo*. Bull. Geoph. Ocean., 63, 325-336, doi: 10.4430/bgo00387.

Belhai D.; 1996: *Évolution tectonique de la zone Ouest algéroise (Ténès-Chenoua): approche stratigraphique et structurale*. Ph.D. thesis. FSTGAT, USTHB, Alger, Algeria, 163 p.

Belhai M., Fujimitsu Y., Bouchareb-Haouchine F.Z., Haouchine A. and Nishijima J.; 2016: *A hydrochemical study of the Hammam Righa geothermal waters in north-central Algeria*. Acta Geochim., 35, 271-287.

Bouchareb-Haouchine F.Z., Boudoukha A. and Haouchine A.; 2012: *Hydrogeochemistry and geothermometry contributions for the identification of the thermal reservoir of Hammam Righa springs, Algeria.* Hydrol. Sci. J., 57, 1184–1195.

Cassiani G., Censini M., Nasta P., Allocca C., Sica B., Lazzaro U., Mazzitelli C., Verdone M., Dani A., Manca di Villahermosa F., Penna D. and Romano N.; 2022: *Time-lapse multi-frequency EMI mapping and ERT profiling for the characterization of soil water behavior in mountain catchments.* In: EGU General Assembly 2022, Vienna, Austria, 23–27 May 2022, EGU22-6956.

Cooley J.W. and Tukey J.W.; 1965: *An algorithm for the machine calculation of complex Fourier series.* Math. Comput., 19, 297-301.

Curewitz D. and Karson J.A.; 1997: *Structural settings of hydrothermal outflow: fracture permeability maintained by fault propagation and interaction.* J. Volcanol. Geotherm. Res., 79, 149-168.

Dahlin T. and Zhou B.; 2004: *A numerical comparison of 2D resistivity imaging with 10 electrode arrays*. Geophys. Prospect., 52, 379-398.

Dastanboo N., Li X.Q. and Gharibdoost H.; 2020: *Comparison between electrical resistivity tomography and tunnel seismic prediction 303 methods for detecting the water zone ahead of the tunnel face: a case study*. Open Geosci., 12, 1094-1104.

Dichiarante A.M., Torgersen E., Redfield T., Köhler A., Torabi A., Svendby K. and Oye V.; 2025: *Spectral analysis of topography as proxy for lineament analysis.* J. Geophys. Res. Solid Earth, 130, e2024JB029790.

Dickson M.H. and Fanelli M.; 2011: *What is geothermal energy?* In: Sørensen B. (ed), Renewable Energy, Earthscan, London, UK, pp. 302-328.

Doghmane M.Z., Ouadfeul S.A. and Aliouane L.; 2022: *Signal analysis*. In: Daya Sagar B.S., Cheng Q., McKinley J. and Agterberg F. (eds), Encyclopedia of Mathematical Geosciences, Encyclopedia of Earth Sciences Series, Springer, Cham, Switzerland, pp. 1288-1297.

Drahor M.G., Berge M.A., Bakak Ö. and Öztürk C.; 2014: *Electrical resistivity tomography monitoring studies at Balçova (Turkey) geothermal site.* Near Surf. Geophys., 12, 337-350.

Durand-Delga M. and Fontboté J.M.; 1980: *Le cadre structural de la Méditerranée occidentale.* In: Géologie des chaînes alpines issues de la Téthys, 26th International Geological Congress, Paris, France, Colloque C5, Mém. BRGM, 115, pp. 67-85.

Gouveia W.P. and Scales J.A.; 1997: *Resolution of seismic waveform inversion: Bayes versus Occam.* Inverse Problems, 13, 323-349.

Griffiths D.H. and Barker R.D.; 1993: *Two-dimensional resistivity imaging and modelling in areas of complex geology*. J. Appl. Geophys., 29, 211-226.

Guigue S.; 1947: *Les sources thermominérales de l'Algérie. Étude géochimique*. Bull. Serv. Carte Géol. Algér., 3e série, 2.

Hernandez J. and Lepvrier C.; 1979: *Le volcanisme calco-alcalin miocène de la région d'Alger (Algérie): pétrologie et signification géodynamique*. Bull. Soc. Géol. Fr., 7, XXI, 73-86.

Hochstein M.P.; 1990: *Classification and assessment of geothermal resources.* In: Dickson M.H. and Fanelli M. (eds), Small geothermal resources: a guide to development and utilization, UNITAR/UNDP Centre on Small Energy Resources, Rome, Italy, pp. 31-57.

Hocine A., Abtout A., Hamai L., Adjiri S. and Mazari A.; 2024: *Hydrothermal system operating mechanism by 3D gravimetric inversion and vertical electrical soundings: case of Hammam Righa hot springs, central Algeria*. J. Afr. Earth Sci., 214, 105268.

Imocha Singh O., Sinam T., James O. and Romen Singh T.; 2012: *Local contrast and mean thresholding in image binarization*. Int. J. Comput. Appl., 51, 4-10.

Issaadi A.; 1992: *Le thermalisme dans son cadre géostructural. Apports à la connaissance de la structure profonde de l'Algérie et de ses ressources géothermales*. Ph.D. thesis, IST, USTHB, Alger, Algeria, 274 pp.

Keller G.V. and Frischknecht F.C.; 1966: *Electrical methods in geophysical prospecting*. Pergamon Press, New York, USA, 519 pp.

Loke M.H.; 1999: *Electrical imaging surveys for environmental and engineering studies: a practical guide to 2-D and 3-D surveys*. Penang, Malaysia.

Loke M.H.; 2002: *RES2DMOD ver. 3.01: rapid 2D resistivity forward modelling using the finite-difference and finite-element methods*. Software manual, Geotomo Software, Malaysia.

Loke M.H., Chambers J.E., Rucker D.F., Kuras O. and Wilkinson P.B.; 2013: *Recent developments in the direct-current geoelectrical imaging method*. J. Appl. Geophys., 95, 135-156.

Maury R.C., Fourcade S., Coulon C., El Azzouzi M., Bellon H., Coutelle A., Ouabadi A., Semroud B., Megartsi M., Cotten J., Belanteur O., Louni-Hacini A., Piqué A., Capdevila R., Hernandez J. and Réhault J.P.; 2000: *Post-collisional Neogene magmatism of the Mediterranean Maghreb margin: a consequence of slab breakoff*. C. R. Acad. Sci. Paris, Ser. IIa, 331, 159-173.

Meghraoui M.; 1988: *Géologie des zones sismiques du nord de l'Algérie: paléosismologie, tectonique active et synthèse sismotectonique*. Ph.D. thesis, Université Paris-Sud, Centre d'Orsay, France, 356 pp.

Ouadfeul S.A. and Aliouane L.; 2023: *Wave-number filtering.* In: Daya Sagar B.S., Cheng Q., McKinley J. and Agterberg F. (eds), Encyclopedia of Mathematical Geosciences, Encyclopedia of Earth Sciences Series, Springer, Cham, Switzerland, pp. 1636-1641, doi: 10.1007/978-3-030-85040-1_349.

Partyka G.; 2005: *Spectral decomposition*. CSEG Recorder, 30(4).

Perrodon A.; 1957: *Étude géologique des bassins néogènes sublittoraux de l'Algérie occidentale*. Bull. Serv. Carte Géol. Algérie, 12, 323 pp.

Ripelin J., Ficheur E. and Brives A.; 1903: *Carte géologique détaillée de l'Algérie*, 62, Marengo. Scale 1:50 000, Service de la carte géologique de l'Algérie, Alger, Algérie.

Qu F., Ren D., Liu X., Jing Z. and Yan L.; 2012: *A face image illumination quality evaluation method based on Gaussian low-pass filter*. In: Proc. 2012 IEEE 2nd International Conference on Cloud Computing and Intelligence Systems (CCIS), Hangzhou, China, pp. 176-180.

Sagar D., Dwivedi S.B. and Basudhar P.K.; 2021: *Electrical resistivity tomography in geotechnical engineering applications*. In: Patel S., Solanki C.H., Reddy K.R. and Shukla S.K. (eds), Proc. Indian Geotechnical Conference 2019, Lecture Notes in Civil Engineering, 133, Springer, Singapore, 157-167.

Saibi H.; 2015: *Geothermal resources in Algeria*. In: Proc. World Geothermal Congress 2015, Melbourne, Australia, International Geothermal Association.

Saibi H., Nishijima J., Aboud E. and Ehara S.; 2006: *Euler deconvolution of gravity data in geothermal reconnaissance; the Obama geothermal area, Japan*. Butsuri-Tansa, 59, 275-282.

Saito H., Hayashi K. and Iikura Y.; 2004: *Detection of formation boundaries and permeable fractures based on frequency-domain Stoneley wave logs*. Geophys. Geophys. Explor., 7, 45-50.

Sanjuan B., Genter A., Fabriol H. and Lachassagne P.; 2004: *Guide de prospection géothermique appliquée aux DOM*. Rapport BRGM/RP-53685-FR, 26 pp.

Saydam A.S. and Duckworth K.; 1978: *Comparison of some electrode arrays for their IP and apparent resistivity responses over a sheet like target*. Geoexploration, 16, 267-289.

Schmidt M.; 2005: *Least squares optimization with L1-norm regularization*. CS542B Project Report, 12 pp.

Setiaji W.A. and Chihping K.; 2023: *Electrical resistivity tomography (ERT) monitoring of groundwater flow condition surround deep excavation in slope area*. IOP Conf. Ser.: Earth Environ. Sci., 1249, 012025.

Sibson R.H.; 1996: *Structural permeability of fluid-driven fault-fracture meshes*. J. Struct. Geol., 18, 1031-1042.

Silversides K.L.; 2020: *Spectral analysis*. In: Daya Sagar B.S., Cheng Q., McKinley J. and Agterberg F. (eds), Encyclopedia of Mathematical Geosciences, Encyclopedia of Earth Sciences Series, Springer, Cham, Switzerland, pp. 1396-1398.

Singha K., Day-Lewis F.D., Johnson T. and Slater L.D.; 2014: *Advances in interpretation of subsurface processes with time-lapse electrical imaging.* Hydrol. Processes, 29, 1549-1576.

Smith S.W.; 1999: *The scientist and engineer's guide to digital signal processing*. *2nd ed.* California Technical Publishing, San Diego, CA, USA, 650 pp.

Stork A.L., Verdon J.P. and Kendall J.-M.; 2014: *The robustness of seismic moment and magnitudes estimated using spectral analysis*. Geophys. Prospect., 62, 862-878, doi: 10.1111/1365-2478.12134.

Tarantola A.; 2005: *Inverse problem theory and methods for model parameter estimation.* Society for Industrial and Applied Mathematics (SIAM), Philadelphia, PA, USA, 342 pp.

Wildi W.; 1983: *La chaîne tello-rifaine (Algérie, Maroc, Tunisie): structure, stratigraphie et évolution du Trias au Miocène*. Rev. Géol. Dyn. Géogr. Phys., 24, 201-297.

Zheng C. and Sun D.-W.; 2008: *Image segmentation techniques.* In: Sun D.-W. (ed), Computer Vision Technology for Food Quality Evaluation, Academic Press, Amsterdam, The Netherlands, pp. 37-56.

Corresponding author: Hadjira Hami
Geophysics Lab, University of Science and Technology Houari Boumediene
BP 32, El Alia, 16111 Bab Ezzouar, Algiers, Algeria
Phone: +213 24 953167; e-mails: hadjira_lon@hotmail.fr, hhami@usthb.dz